

Research Article

Marwan Gebran*, Frederic Paletou, Ian Bentley, Rose Brienza, and Kathleen Connick

Deep learning applications for stellar parameter determination: II-application to the observed spectra of AFGK stars

<https://doi.org/10.1515/astro-2022-0209>
received June 27, 2022; accepted October 25, 2022

Abstract: In this follow-up article, we investigate the use of convolutional neural network for deriving stellar parameters from observed spectra. Using hyperparameters determined previously, we have constructed a Neural Network architecture suitable for the derivation of T_{eff} , $\log g$, $[M/H]$, and $v_e \sin i$. The network was constrained by applying it to databases of AFGK synthetic spectra at different resolutions. Then, parameters of A stars from Polarbase, SOPHIE, and ELODIE databases are derived, as well as those of FGK stars from the spectroscopic survey of stars in the solar neighbourhood. The network model's average accuracy on the stellar parameters is found to be as low as 80 K for T_{eff} , 0.06 dex for $\log g$, 0.08 dex for $[M/H]$, and 3 km/s for $v_e \sin i$ for AFGK stars.

Keywords: data analysis methods, statistical, methods, deep learning methods, spectroscopic techniques, fundamental parameter stars

1 Introduction

Artificial intelligence (AI) is becoming a vital tool in science due to its automation capabilities and its capacity to handle large amounts of data. In the context of astronomy, a subset of AI, machine learning (ML), and deep learning (DL) are extensively used for ground-based and sky surveys

(Baron 2019). In our previous work, Gebran *et al.* (2022) (hereafter referred to as Paper I), we constructed a deep neural network (DNN) in order to derive stellar parameters,¹ such as effective temperature (T_{eff}), surface gravity ($\log g$), metallicity ($[M/H]$), and the projected equatorial rotational velocity ($v_e \sin i$), for B and A stars. In Paper I, we constrained most of the hyperparameters utilized in the construction of NN in order to ensure that the best accuracy for deriving stellar labels could be achieved.

Many tools and techniques are being developed to derive the fundamental parameters of stars, and most of them are either based on statistical or ML/DL approaches. A thorough list of the most updated studies can be found in the Introduction of Paper I. Recently, Li *et al.* (2022b) used a combination of least absolute shrinkage and selection operator and multilayer perceptron (MLP) methods to estimate stellar atmospheric parameters from the large sky area multi-object fiber spectroscopic telescope (LAMOST) DR8 low-resolution spectra. Straumit *et al.* (2022) presented a spectral analysis algorithm, ZETA-PAYNE, developed to obtain stellar labels from the fifth Sloan Digital Sky Survey spectra of stars of OBAF spectral types using ML tools. Li *et al.* (2022a) applied an ML technique, the Gaussian process (GP) regression, to turn a sparse model grid into a continuous function. They also used the GP regression to determine the age and mass of stars. Kjærsgaard *et al.* (2021) presented an NN autoencoder approach for extracting a telluric transmission spectrum from a large set of high-precision observed solar spectra from the high accuracy radial velocity planet searcher (HARPS-N) radial velocity spectrograph. Hu *et al.* (2022) presented a data-driven method based on Long Short-Term Memory neural networks to analyze the spectral time series of Type Ia supernovae (SN Ia). Their method allows for accurate reconstruction of the spectral sequence of an SN Ia based on a single observed spectrum around maximum light. More recently, Xiong *et al.*

* **Corresponding author: Marwan Gebran**, Department of Chemistry and Physics, Saint Mary's College, Notre Dame, IN 46556, USA, e-mail: mgebrane@saintmarys.edu

Frederic Paletou: Irap, Université de Toulouse, Observatoire Midi-Pyrénées, CNRS, CNES, 14 av. E. Belin, F-31400 Toulouse, France

Ian Bentley, Rose Brienza, Kathleen Connick: Department of Chemistry and Physics, Saint Mary's College, Notre Dame, IN 46556, USA

¹ When dealing with DNN, stellar parameters are often called stellar labels.

(2022) presented a residual recurrent neural network to extract spectral information and estimate stellar atmospheric parameters along with 15 chemical element abundances for medium-resolution spectra from LAMOST.

Most of the automated techniques that are found in the literature deal with the derivation of the fundamental parameters (T_{eff} , $\log g$, and $[M/H]$) without considering $v_e \sin i$. Rotational profiles are usually found by applying transformations such as the Fourier transform (Zorec and Royer 2012) or using rotational laws (Zorec *et al.* 2017). In our previous studies (Aydi *et al.* 2014, Gebran *et al.* 2016, Kassounian *et al.* 2019, Gebran *et al.* 2022), we have derived $v_e \sin i$ using line profile fitting.

In this work, we complement the study of Paper I by using its best combination of hyperparameters to find the best NN architecture. The foremost purpose of our study is to develop a consistent model that is capable of predicting accurate and precise stellar parameters, which is a guiding starting point for most stellar physics projects. Of course, other sources of uncertainty can affect the predicted results when applied to real observations, as will be discussed in this article. Once the architecture and parameters are set, we applied our technique to AFGK observed spectra (Gebran *et al.* 2016, Kassounian *et al.* 2019, Paletou *et al.* 2015).

The construction of the training databases is explained in Section 2. The preprocessing steps are detailed in Section 3. The construction of the NN model with all the details is discussed in Section 4. The application of the method to AFGK stars is found in Section 5. The discussion and conclusion can be found in Section 6.

2 Training databases

A grid of 12 training databases was constructed for the purpose of this study. Other than modifying the stellar labels (T_{eff} , $\log g$, and $[M/H]^2$, $v_e \sin i$), we have constructed a series of grids with the same range of stellar labels but at different resolving powers. The purpose is to analyze the effect of resolution on the accuracy of the derived stellar label and to check the capability of our technique when applied to low-, medium-, and high-resolution spectrometers.

We have followed the same strategy as in Paper I. We have first calculated a series of ATLAS9 (Kurucz 1992) model atmospheres using the opacity distribution function of

Castelli and Kurucz (2003) and with a mixing length parameter of 0.5 for $7,000 \text{ K} \leq T_{\text{eff}} \leq 8,500 \text{ K}$, and 1.25 for $T_{\text{eff}} \leq 7,000 \text{ K}$ (Smalley 2004). Using SYNSPEC48 (Hubeny and Lanz 1992), we have calculated synthetic spectra for AFGK stars. We ended up with a grid of 80,000 synthetic spectra, for each resolving power, with parameters ranging randomly between the values described in Table 1. We have used the same line list as the one used in Paper I. The wavelength range was selected to be between 4,450 and 5,400 Å. This wavelength range is indeed very sensitive to all stellar parameters in the spectral range of AFGK stars (Paletou *et al.* 2015, Gebran *et al.* 2016, Kassounian *et al.* 2019, Gebran *et al.* 2022). This region is also insensitive to microturbulent velocity, which was adopted to be $\xi_t = 2 \text{ km/s}$ for A stars and $\xi_t = 1 \text{ km/s}$ for FGK stars (Gebran *et al.* 2016, 2014). An example of the calculated spectra for different resolving powers is displayed in Figure 1.

3 Principal component analysis (PCA) for preprocessing

Before applying the NN to the training database, a dimension reduction technique is applied. This step consists in reducing the size of the spectra from a sampling size of N_k to $n_k < N_k$. Depending on the resolving power, N_k ranges between 4,750 and 19,000 data points. The n_k reduced data points are found by projecting the flux of each spectrum onto the first 50 principal components (PCs). Technically, we apply this PCA on the training database and find the eigenvectors $\mathbf{e}_k(\lambda)$ of the variance–covariance matrix \mathbf{C} :

$$\mathbf{C} = (\mathbf{M} - \bar{\mathbf{M}})^T \cdot (\mathbf{M} - \bar{\mathbf{M}}), \quad (1)$$

Table 1: Ranges of the parameters used for the calculation of the training databases

Parameters	Range	Step
T_{eff} (K)	[4,000, 11,000]	50
$\log g$ (dex)	[2.0, 5.0]	0.05
$[M/H]$ (dex)	[−1.5, 1.5]	Random
$v_e \sin i$ (km/s)	[0, 300]	Random
λ (Å)	4,450–5,400	λ Resolving power

The third column displays the steps in the parameter range. Note that the steps in T_{eff} and $\log g$ are the steps in ATLAS9 model atmospheres. Many databases were constructed for different resolving powers ranging from 1,000 to 115,000. Random step means that there is no restriction on the number selection.

² $[M/H]$ refers to an overall metallicity and not to the iron abundance. All elemental abundances are scaled according to $[M/H]$.

where the training database \mathbf{M} is an $N_{\text{spectra}} \times N_{\lambda}$ matrix containing the fluxes of the synthetic spectra. The value of n_k is found by analyzing the reconstructed error (Gebran *et al.* 2022). Having $n_k = 50$ reduces the mean reconstructed error to a value less than 0.5%. As a similar technique to PCA, one could also use the encoder part of an autoencoder in order to reduce the dimensionality of the database (Kjærsgaard *et al.* 2021). We have chosen PCA to be consistent with our previous findings in Gebran *et al.* (2016, 2022).

4 DL

We start by applying data augmentation as a regularization technique to all the training databases (see Section 4.1.1 of Paper I for technical explanations). This is done in

order to take into account the noise in the real observed spectra and some modifications that could occur in the shape of the observed spectra due to bad normalization or inappropriate data reduction. Every spectrum (including the augmented ones) in each database is represented by 50 data points, and they correspond to a specific T_{eff} , $\log g$, $[M/H]$, and $v_e \sin i$. This is true of all resolving powers. An NN is then used to link these data points to their corresponding labels. Four different NNs were built, one for each stellar label (T_{eff} , $\log g$, $[M/H]$, $v_e \sin i$).

The initializers, optimizers, learning rates, dropout fraction, pooling layers, activation functions, loss functions, epochs, and batches are constrained according to the methodology of Paper I. These network parameters were derived for every network architecture tested in this work.

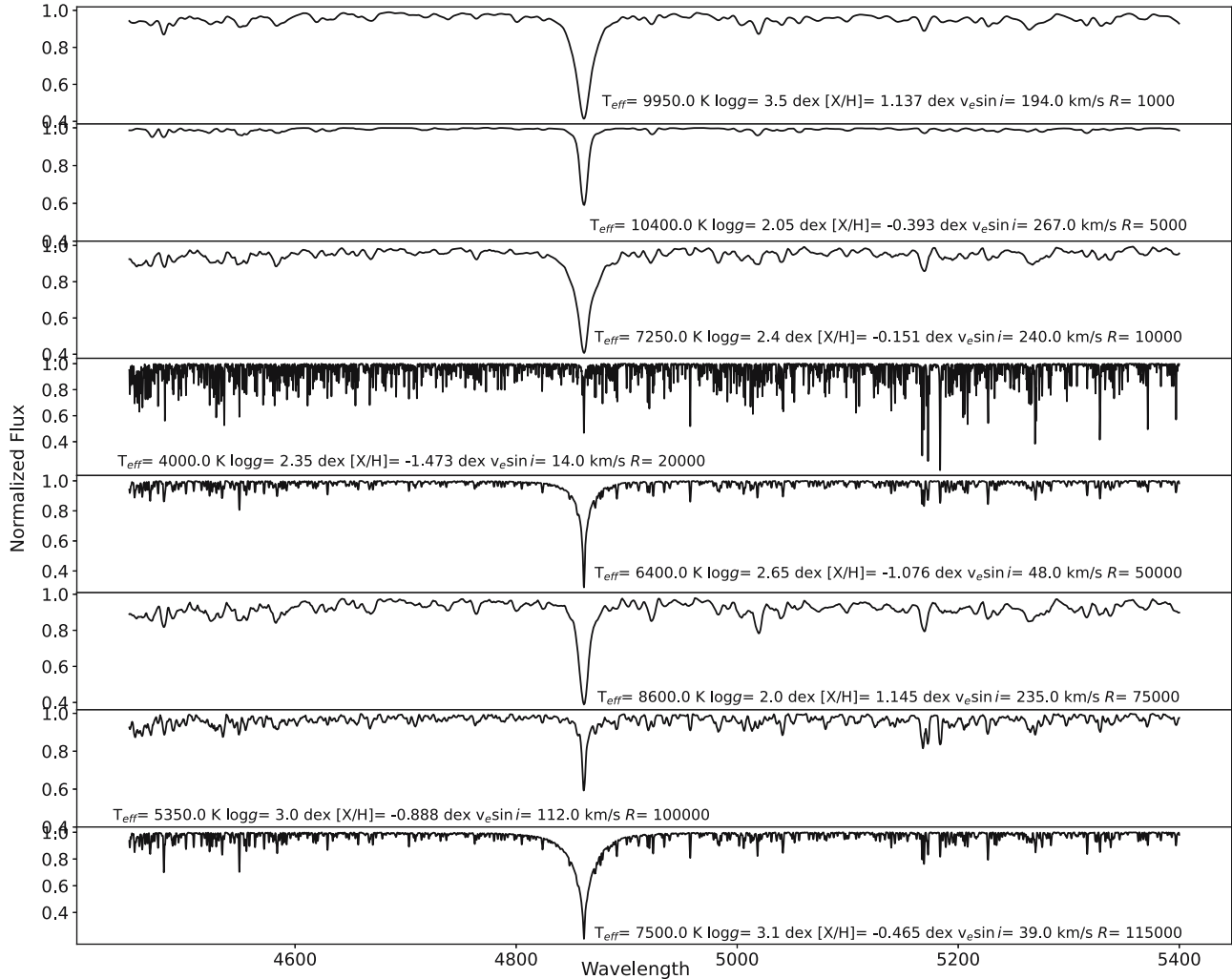


Figure 1: Sample of synthetic spectra calculated with different stellar parameters and spectral resolutions. These noise-free spectra are normalized to the local continuum.

4.1 Architecture

An infinite number of architectures could be applied to our purpose. The main goal is to find the most accurate transformation between the matrix of spectral coefficients (the 50 projected ones) and the labels. The best architecture will be selected according to its simplicity (size and calculation time) and the accuracy of the results.

Fully dense NNs, Convolutional Neural Networks (CNN), and a combination of both were tested for each stellar label. In each case, we have iterated on the number of layers, and number of neurons in each layer, and the size of the filters in the case of CNNs. As explained previously, network parameters were derived for each NN.

For every network and every resolving power, each augmented database was divided into 70% for training, 20% for validation, and 10% for testing. Gaussian signal-to-noise ratio was selected randomly between 5 and 300 and applied to each spectrum of the 10% test spectra in order to check the accuracy of the technique on noisy data.

All our calculations are performed using the open-source programming language, Python, specifically with the Keras³ interface on the TensorFlow⁴. We have used the KerasTuner⁵ package (O'Malley *et al.* 2019), a scalable hyperparameter optimization framework that solves the pain points of hyperparameter search. It was used to derive the optimized number of layers as well as the filter sizes in the case of CNNs. Linking the number of layers and dimensions of the filters with the size of the database as well as the size of each spectrum in the database is not an easy task. In order to avoid over- and under-fitting, these two parameters should be optimized. KerasTuner helps in that regard and avoids the hassle of the time-consuming trial and error phase.

After iterating on the architecture shape and deriving the optimized parameters for each network, the result was a unique architecture that is applicable to all stellar parameters. Figure 2 shows the architecture of NN for deriving T_{eff} . This architecture is similar for predicting $\log g$, $[M/H]$, and $v_e \sin i$. Although the four parameters are predicted for networks having similar architecture, these models differ in the activation function, the kernel initializer, the loss function, the optimizer, the dropout fraction, the epoch, and the batch number (Gebran *et al.* 2022). The adopted values for the network parameters are

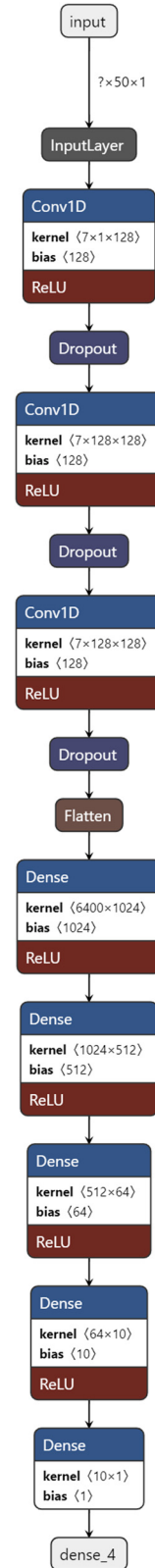


Figure 2: Neural network architecture used in this study for predicting T_{eff} , $\log g$, $[M/H]$, and $v_e \sin i$. These parameters are predicted with networks having the same architecture but different parameters as shown in Table 2. Explanations about the kernel and bias dimensions can be found in the study by Wu (2017).

³ <https://keras.io/>.

⁴ <https://www.tensorflow.org/>.

⁵ https://keras.io/keras_tuner/.

Table 2: Set of parameters used for the four networks, for deriving T_{eff} , $\log g$, $[M/H]$, and $v_e \sin i$; these parameters are derived using the technique explained in Paper I

Parameter	T_{eff}	$\log g$	$[M/H]$	$v_e \sin i$
Kernel initializer	he_normal	he_normal	Random uniform	he_uniform
Loss function	Mean squared logarithmic error	Mean squared logarithmic error	Mean absolute error	Mean squared error
Optimizer	Adam	Adamax	Adam	Adamax
Epochs	350	75	75	75
Batch	128	128	32	64
Activation function	Relu	tanh	tanh	tanh
Dropout fraction	0.3	0.3	0.2	0.3

derived using the technique explained in Paper I. These parameters are summarized in Table 2.

4.2 Resolution effect

Spectroscopic surveys are based on instruments that have different resolving powers. For that reason, we have applied our technique to different databases that are similar in parameter ranges (Table 1), except for the resolving power. Our tests contain spectra with a low resolution down to 1,000 and a high resolution of up to 115,000.

Once the networks are trained using 70% of the data, we have derived the accuracy of the parameters for the validation, test, and noisy test data. The best accuracy reached as a function of the resolution is displayed in Figure 3. For each stellar label, the derived accuracy for the noisy test data is representative of the error bar that should be assigned to the observed spectra. For example, when analyzing spectra at a resolving power of 50,000, the equatorial projected rotational velocity should be assigned an error $\sigma_{v_e \sin i_m} \sim 2.5$ km/s. The subscript m corresponds to the fact that this is model related. For a resolving power larger than 5,000, the accuracy values are always in the same order, and their average is 80 K for T_{eff} , 0.06 dex for $\log g$, 0.08 dex for $[M/H]$, and 3 km/s for $v_e \sin i$.

5 Application to observed spectra

After the four networks were applied to synthetic data and the architecture and parameters found, we used them to predict the stellar parameters from *observed* spectra. We used well-studied AFGK stars observed with different instruments at different resolutions. Applying the predictions to observed spectra assumes that the radiative transfer code is

able to produce synthetic spectra similar to the observed ones using the specific stellar parameters. We have shown in previous studies (Gebran *et al.* 2016, Kassounian *et al.* 2019) that SYNSPEC48 was able to reproduce the spectra of AFGK stars with good accuracy, but other reliable synthetic spectra codes could be used if needed. We can mention the PHOENIX models (Husser *et al.* 2013) that are well suited for stars having $T_{\text{eff}} \leq 12,000$ K or TURBOSPECTRUM (Plez 2012) with all the molecular data that are used for giant and dwarf stars.

For the A stars, we used the list of Gebran *et al.* (2016) and selected the ones that have the most values published in the literature. We ended up with 89 observed A stars with more than nine values for T_{eff} in the VizieR catalog. These A stars were observed with NARVAL and ESPaDOnS high-resolution spectropolarimeters, which have a spectral resolving power of 65,000 in polarimetric mode and 76,000 when used for spectroscopy. These spectra were retrieved from PolarBase (Petit *et al.* 2014), a high-resolution spectropolarimetric stellar observations database. Another part of the A stars spectra was observed with the ELODIE (Baranne *et al.* 1996, Moutaka *et al.* 2004) and SOPHIE (Perruchot *et al.* 2011, Illovaisky *et al.* 2008) spectrographs with a resolving power of 42,000 and 75,000, respectively. Details about the observations can be found in Gebran *et al.* (2016) and Kassounian *et al.* (2019). For the FGK stars, we have used 96 stellar spectra from the Spectroscopic Survey of Stars in the Solar Neighbourhood (S^4N , Allende Prieto *et al.* 2004), analyzed in Paletou *et al.* (2015) with a resolving power of 50,000. As done in our previous studies (Paletou *et al.* 2015, Gebran *et al.* 2016), variable or active stars, showing time-emission features of changing strength/amplitude were excluded.

For each resolving power, we used the corresponding trained NN model. To do that, the observations were corrected for the radial velocity shift using the classical cross-correlation technique (Tonry and Davis 1979). The spectra are then interpolated in the wavelength range

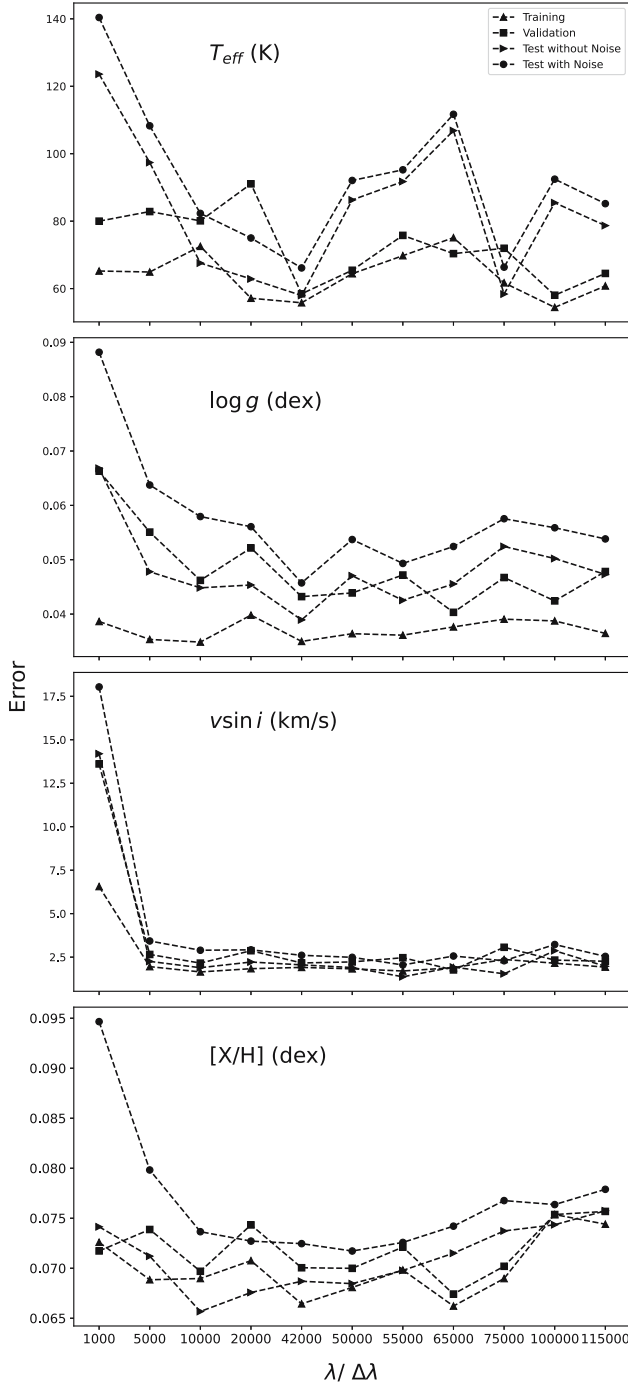


Figure 3: Derived accuracy for T_{eff} , $\log g$, $[M/H]$, and $v_e \sin i$ as a function of the resolving power. We present the accuracy values for the training data (triangles), the validation data (squares), the test data (triangles tilted right), and the noisy test data (circles).

used during the training, between 4,450 and 5,400 Å for A stars and 5,000–5,400 Å for FGK stars. The wavelength range of the S⁴N observations is smaller than that of A stars. For that reason, a reduced database with a smaller wavelength range was interpolated from the original one

at 50,000 resolving power and was used for these specific FGK stars. Then, all observed spectra were projected into their corresponding PCs and the first 50 data points were conserved for the prediction.

5.1 AFGK stars

Predicted stellar parameters are depicted in Tables A1 and A2 in the Appendix. In these tables, the stellar parameters are represented with the median and closest values retrieved from VizieR catalogs using astroquery⁶ (Paietou and Zolotukhin 2014)⁷.

Figure 4 shows the predicted effective temperature of a sample of stars, as well as the range in the effective temperatures retrieved from the catalogs (boxplots) and the median. The selection of these stars was based on the number of values found in the literature. For A stars, we have selected the ones that have more than 20 different values in VizieR. As for FGK stars, we did the same with stars having more than 100 independent literature values for T_{eff} . Figures 5–7 are similar to Figure 4 but for $\log g$, $[M/H]$, and $v_e \sin i$. A stars in Figure 5 have more than ten cataloged values for $\log g$ and F stars have more than 50. For $[M/H]$ and $v_e \sin i$, we have chosen the A stars that have more than ten cataloged values for these two parameters. For FGK stars, we have selected the ones having more than 50 and 15 values for $[M/H]$ and $v_e \sin i$, respectively.

A large spread exists in the literature for all parameters. To estimate the accuracy of our results, we used a weighted mean approach similar to the one described in Gebran *et al.* (2016). Quantitatively, and in order to give more weight to the cataloged values that have a large number of occurrences and a small spread in values, the dispersion and its corresponding standard deviation for a stellar parameter X are calculated as follows:

$$\Delta X = \frac{\sum_i w_i (X^{\text{prediction}} - X^{\text{median}})}{\sum_i w_i},$$

where

$$w_i = \frac{1}{\text{IQR}_i},$$

IQR_i being the interquartile range defined as the difference between the third and first quartiles of each set of values. The standard deviation is calculated as follows:

⁶ <https://astroquery.readthedocs.io>.

⁷ <https://arxiv.org/abs/1408.7026>.

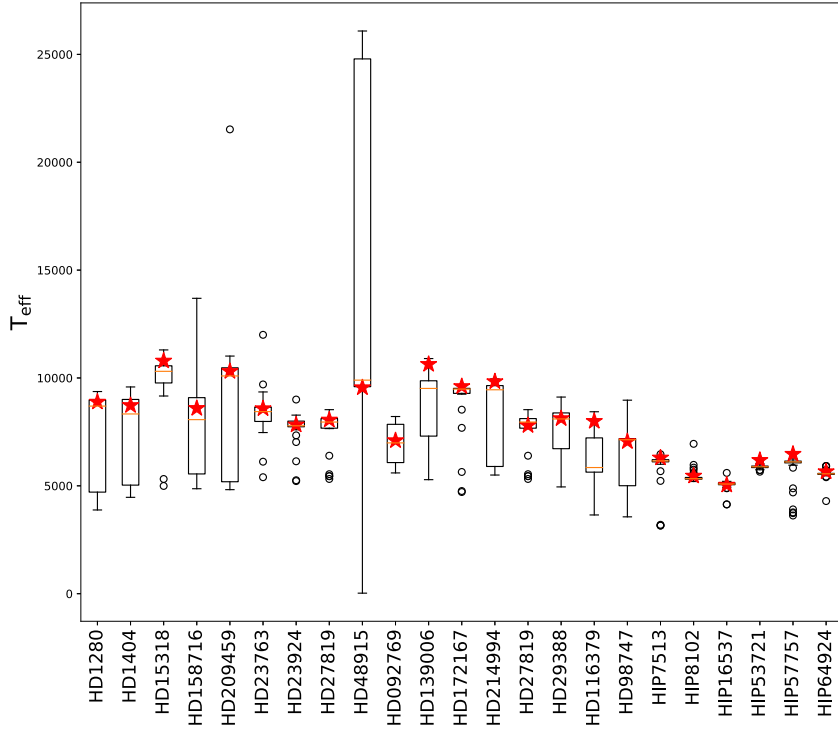


Figure 4: Comparison between our predicted effective temperatures (stars), and the values we obtained from available Vizier catalogs. The cataloged values are represented as classical boxplots. The objects we studied are listed along the horizontal axis. The horizontal bar inside each box indicates the median (Q_2 value), while each box extends from the first quartile, Q_1 , to the third quartile Q_3 . Extreme values, still within 1.5 times the interquartile range away from either Q_1 or Q_3 , are connected to the box with dashed lines. Outliers are denoted by an “o” symbol.

$$\sigma_X = \left[\frac{\sum_i w_i (X^{\text{prediction}} - X^{\text{median}})^2}{\sum_i w_i} \right]^{\frac{1}{2}}.$$

Stars having only one cataloged value for a specific parameter were not considered in the calculation of the dispersion. The results of the dispersion as well as the standard deviations are displayed in Table 3. Cataloged values are all coming from different sources, and each author uses a different technique (photometry, spectroscopy, spectrophotometry, asteroseismology, *etc.*). This leads to a large dispersion and a large deviation between our predicted values and the ones in the literature. A better way to estimate this dispersion is to do a comparison with the sample used in Figures 4–7. This sample contains the stars having the largest number of independent cataloged values. The new dispersion and standard deviations are displayed in Table 3 depicted with the “lim” subscript. In that case, the dispersion reduces drastically, reaching an average of 150 K, 0.01 dex, 0.04 dex, and 3.0 km/s for T_{eff} , $\log g$, $[M/H]$, and $v_e \sin i$, respectively, and with smaller standard deviation than in the case of the whole sample.

The dispersion found between our predicted $v_e \sin i$ for FGK and the ones in the literature is mainly explained by the fact that our $v_e \sin i$ include the macroturbulence effects,

whereas some of the authors derive both parameters separately (see, *e.g.*, Allende Prieto *et al.* 2004). In the case of A stars, the $v_e \sin i$ values for every sharp-lined spectra (*e.g.*, $v_e \sin i \leq 5$ km/s) should be considered as upper limits because, macroturbulence effect is neglected. For moderate and fast rotators, macroturbulence has no significant effect on the line shape (Takeda *et al.* 2018, Frémat *et al.* 2022). When only considering A stars, Δ_{lim} and σ_{lim} of Table 3 become 1.3 and 5.0 km/s, respectively. These results show that we are able to recover the stellar parameters of AFGK stars with good accuracy using our trained models. However, as explained in Paper I, the size of the database is very crucial for the convergence of the model as well as for the recovered accuracy of the stellar parameter. The size of the database depends on many factors, including the spectral type of the stars, the wavelength range, and the type of predicted parameters. We have used a database of $\sim 80,000$ spectra in our study but this number should be monitored.

6 Discussion and conclusion

Two sources of errors should be assigned to the predicted stellar parameters. One relates to the model ($\sigma_{\text{parameter}_m}$,

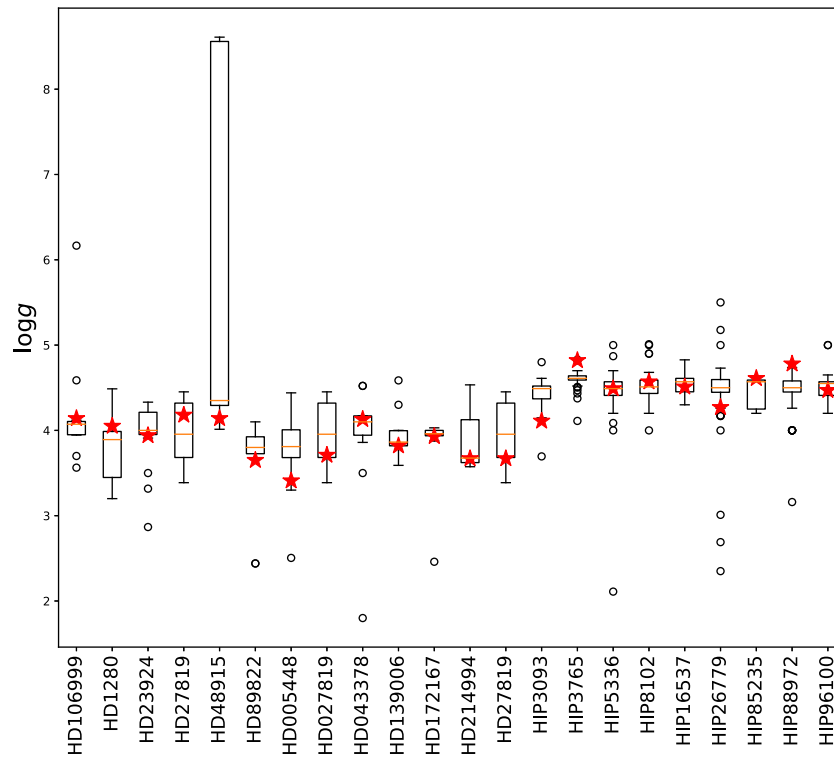


Figure 5: Same as Figure 4 but for $\log g$.

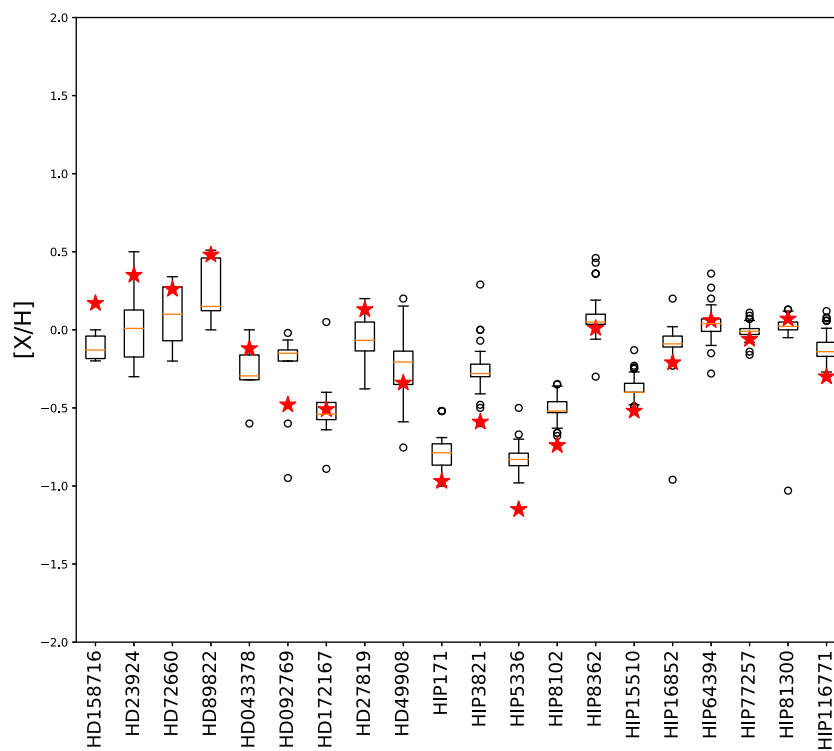


Figure 6: Same as Figure 4 but for $[M/H]$.

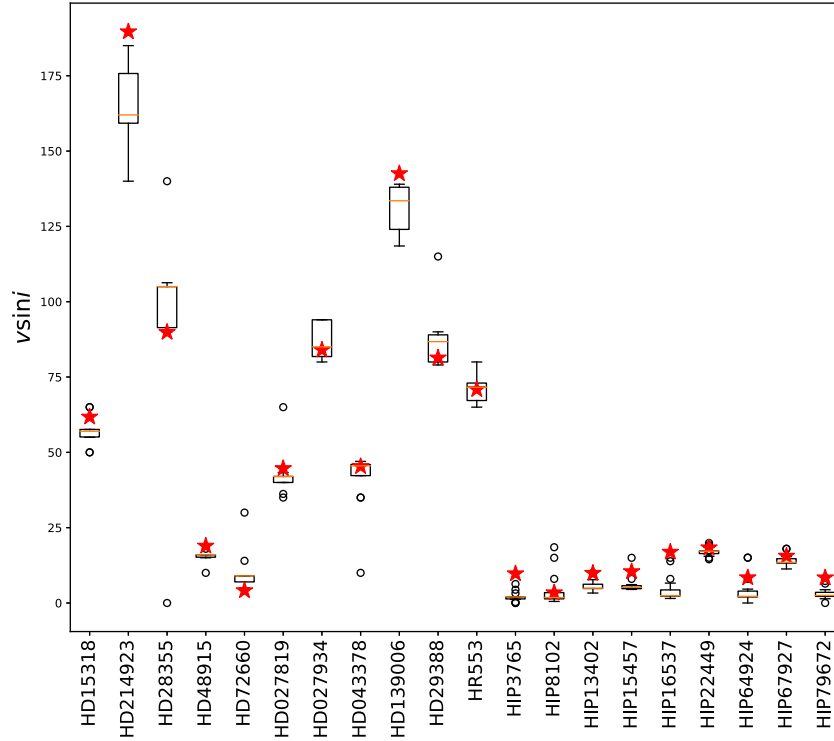


Figure 7: Same as Figure 4 but for $v_e \sin i$.

Table 3: Dispersion and standard deviation for the comparison between our predicted parameters and the cataloged ones

	T_{eff} (K)	$\log g$ (dex)	$[M/H]$ (dex)	$v_e \sin i$ (km/s)
Δ	160	0.40	0.15	12
σ	300	0.55	0.35	15
Δ_{lim}	150	0.01	0.04	3.0
σ_{lim}	250	0.15	0.14	5.5

The last two rows deal with a limited cataloged sample, the one used to plot Figures 4–7.

Section 4.2) and the other relates to how close the radiative transfer code (*i.e.*, SYNSPEC48, $\sigma_{\text{parameter}_{\text{rtc}}}$) represents the observations. $\sigma_{\text{parameter}_{\text{rtc}}}$ can be derived using a list of well-studied stars with well-established stellar parameters over a wide range in the Hertzsprung-Russell Diagram. It is beyond the scope of this study, but we should be aware that this source of error could be wavelength dependant as each radiative transfer code uses a different line list with different atomic data.

Model (*i.e.*, NN) and radiative transfer errors are independent and can be added in a quadratic manner to find the total accuracy that we found in Section 5.1:

$$\sigma_{\text{parameter}_{\text{total}}} = (\sigma_{\text{parameter}_m}^2 + \sigma_{\text{parameter}_{\text{rtc}}}^2)^{\frac{1}{2}}.$$

While comparing with the median values from the literature, we found that T_{eff} is derived with an accuracy of 150 K, $\log g$ with 0.01 dex, $[M/H]$ with 0.04 dex, and $v_e \sin i$ with 3.0 km/s. Some of these deviations are smaller than the errors found in the model (80 K for T_{eff} , 0.06 dex for $\log g$, 0.08 dex for $[M/H]$, and 3.0 km/s for $v_e \sin i$), but one should consider the accuracy of the model as a minimum limit for the stellar parameters and then calculate the total accuracy depending on the radiative transfer code specificity.

We have used a large range of spectral types and found acceptable values for accuracy. One could use a combination of a stellar library with synthetic data adapted for each spectral type and luminosity range or a large database of observed stars with accurate stellar parameters. However, NN proves to be a fast (refer to Paper I for computational time) and accurate way to derive stellar parameters and can handle a large amount of data. These results are very promising, as they are less accurate than those usually found with photometric techniques (Smalley 2005, Jin-Meng *et al.* 2021, Green *et al.* 2021), spectroscopic ones (Gill *et al.* 2018, Gebran *et al.* 2016, Ting *et al.* 2019, Kassounian *et al.* 2019, Tabernero *et al.* 2022), or a combination of both (Adelman *et al.* 2002, Heiter *et al.* 2015).

In future work, we will be testing the effect of specific spectral regions on the stellar parameters. This will be done through autoencoders, a type of unsupervised learning technique, leading to a more “intelligent” and compact database construction.

One straightforward application is the use of such a network in order to derive the stellar parameters of Gaia spectra (Collaboration *et al.* 2016). The radial velocity spectrometer (Cropper *et al.* 2018) on board of Gaia will deliver medium-resolution spectra ($R \sim 11,000$) in the CaII triplet region (λ ranging from 8,470 to 8,710 Å). Several millions of stars have their spectra available during the Data Release 3 (DR3, Collaboration *et al.* 2022, Frémat *et al.* 2022).

Acknowledgement: We are very grateful to the referees of the article for their useful remarks.

Funding information: This work was supported by the Neuhoﬀ Summer Research Scholarship program at Saint Mary’s College.

Author contributions: All authors have accepted responsibility for the entire content of this manuscript and approved edits submission.

Conflict of interest: The authors state that there is no conflict of interest.

References

- Adelman SJ, Pintado OI, Nieva MF, Rayle KE, Sanders SE. 2002. On the effective temperatures and surface gravities of superficially normal main sequence band B and A stars. *A&A*. 392:1031–1037.
- Allende Prieto C, Barklem PS, Lambert DL, Cunha K. 2004. S^4N : A spectroscopic survey of stars in the solar neighborhood. The Nearest 15 pc. *A&A*. 420:183–205.
- Aydi E, Gebran M, Monier R, Royer F, Lobel A, Blomme R. 2014. Automated procedure to derive fundamental parameters of B and A stars: Application to the young cluster NGC 3293. In: Ballet J, Martins F, Bournaud F, Monier R, Reylé, C, editors, *SF2A-2014: Proceedings of the Annual meeting of the French Society of Astronomy and Astrophysics*; 2014 Jun 3–6; Paris, France. Paris: SF2A. p. 451–455.
- Baranne A, Queloz D, Mayor M, Adrianzyk G, Knispel G, Kohler D, et al. 1996. Elodie: A spectrograph for accurate radial velocity measurements. *Astron. Astrophys. Suppl. Ser.* 119(2):373–390.
- Baron D. 2019. Machine Learning in Astronomy: a practical overview. *arXiv e-prints*, arXiv:1904.07248.
- Castelli F, Kurucz RL. 2003. New grids of ATLAS9 model atmospheres. In: Piskunov N, Weiss WW, Gray DF, editors, *Proceedings of the 210th Symposium of the International Astronomical Union held at Uppsala University, Uppsala, Sweden, 17–21 June, 2002*. IAU by the Astronomical Society of the Pacific. p. A20.
- Cropper M, Katz D, Sartoretti P, Prusti T, de Bruijne JHJ, Chassat F, et al. 2018. Gaia data release 2. Gaia radial velocity spectrometer. *A&A*. 616:A5.
- Frémat Y, Royer F, Marchal O, Blomme R, Sartoretti P, Guerrier A, et al. 2022. Gaia Data Release 3: Properties of the line broadening parameter derived with the radial velocity spectrometer (RVS). *arXiv e-prints*, arXiv:2206.10986.
- Gaia Collaboration, Creevey OL, Sarro LM, Lobel A, Pancino E, Andrae R, et al. 2022. Gaia Data Release 3: A Golden Sample of Astrophysical Parameters. *arXiv e-prints*, arXiv:2206.05870.
- Gaia Collaboration, Prusti T, de Bruijne JHJ, Brown AGA, Vallenari A, Babusiaux C, et al. 2016. The Gaia mission. *A&A*. 595:A1.
- Gebran M, Connick K, Farhat H, Paletou F, Bentley I. 2022. Deep learning application for stellar parameters determination: I-constraining the hyperparameters. *Open Astron.* 31(1):38–57.
- Gebran M, Farah W, Paletou F, Monier R, Watson V. 2016. A new method for the inversion of atmospheric parameters of A/Am stars. *A&A*. 589:A83.
- Gebran M, Monier R, Royer F, Lobel A, Blomme R. 2014. Microturbulence in A/F Am/Fm stars. In: Mathys G, Griffin ER, Kochukhov O, Monier R, Wahlgren GM, editors, *Putting A Stars into Context: Evolution, Environment, and Related Stars*, *Proceedings of the International Conference, Moscow: Publishing House “Pero”*. p. 193–198.
- Gill S, Maxted PFL, Smalley B. 2018. The atmospheric parameters of FGK stars using wavelet analysis of CORALIE spectra. *A&A*. 612:A111.
- Green GM, Rix H-W, Tschesche L, Finkbeiner D, Zucker C, Schlafly EF, et al. 2021. Data-driven stellar models. *ApJ*. 907(1):57.
- Heiter U, Jofré P, Gustafsson B, Korn AJ, Soubiran C, Thévenin F. 2015. Gaia FGK benchmark stars: Effective temperatures and surface gravities. *A&A*. 582:A49.
- Hu L, Chen X, Wang L. 2022. Spectroscopic studies of type Ia supernovae using LSTM neural networks. *ApJ*. 930(1):70.
- Hubeny I, Lanz T. 1992. Accelerated complete-linearization method for calculating NLTE model stellar atmospheres. *A&A*. 262(2):501–514.
- Husser TO, Wende-vonBerg S, Dreizler S, Homeier D, Reiners A, Barman T. et al. 2013. A new extensive library of PHOENIX stellar atmospheres and synthetic spectra. *A&A*. 553:A6.
- Ilovaisky S, Prugniel P, Soubiran C, Koleva M, Le Coroller H. 2008. The ELODIE-SOPHIE archive in the virtual observatory. In: Guainazzi M, Osuna P, editors, *Astronomical Spectroscopy and Virtual Observatory, Proceedings of the EURO-VO Workshop, held at the European Space Astronomy Centre of ESA, Villafranca del Castillo, Spain, European Space Agency*. p. 47.
- Jin-Meng Y, Xiao-Qing W, Min Z. 2021. The regression of effective temperatures in APOGEE and LAMOST. *New Astron.* 86:101568.
- Kassounian S, Gebran M, Paletou F, Watson V. 2019. Sliced Inverse Regression: application to fundamental stellar parameters. *Open Astron.* 28(1):68–84.
- Kjærsgaard RD, Bello-Arufe A, Rathcke AD, Buchhave LA, Clemmensen LKH. 2021. Unsupervised Spectral Unmixing for Telluric Correction Using a Neural Network Autoencoder. *arXiv e-prints*, arXiv:2111.09081.

- Kurucz RL. 1992. Atomic and molecular data for opacity calculations. *RMXAA*. 23:45.
- Li T, Davies GR, Lyttle AJ, Ball WH, Carboneau LM, García RA. 2022a. Modelling stars with Gaussian process regression: augmenting stellar model grid. *MNRAS*. 511(4):5597–5610.
- Li X, Wang Z, Zeng S, Liao C, Du B, Kong X, et al. 2022b. Estimation of stellar atmospheric parameters from LAMOST DR8 low-resolution spectra with $20 \leq \text{SNR} < 30$. arXiv e-prints, arXiv:2204.06301.
- Moultaka J, Ilovaisky SA, Prugniel P, Soubiran C. 2004. The ELODIE archive. *PASP*. 116(821):693–698.
- O'Malley T, Bursztein E, Long J, Chollet F, Jin H, Invernizzi L, et al. 2019. KerasTuner. <https://github.com/keras-team/keras-tuner>.
- Paletou F, Böhm T, Watson V, Trouilhet JF. 2015. Inversion of stellar fundamental parameters from ESPaDOnS and Narval high-resolution spectra. *A&A*. 573:A67.
- Paletou F, Zolotukhin I. 2014. Using virtual observatory with python: querying remote astronomical databases. arXiv e-prints, arXiv:1408.7026:1408.7026.
- Perruchot S, Bouchy F, Chazelas B, Dilliaz RF, Hébrard G, Arnaud K, et al. 2011. Higher-precision radial velocity measurements with the SOPHIE spectrograph using octagonal-section fibers. In: Shaklan S, editor, *Techniques and Instrumentation for Detection of Exoplanets V*, vol 8151 of Society of Photo-Optical Instrumentation Engineers (SPIE) Conference Series, p. 815115.
- Petit P, Louge T, Théado S, Paletou F, Manset N, Morin J, et al. 2014. PolarBase: a database of high-resolution spectropolarimetric stellar observations. *PASP*. 126(939):469.
- Plez B. 2012. Turbospectrum: Code for spectral synthesis. *Astrophys. Source Code Library record ascl:1205.004*.
- Smalley B. 2004. Observations of convection in A-type stars. In: Zverko J, Ziznovsky J, Adelman SJ, Weiss WW, editors, *The A-Star Puzzle held in Poprad, Slovakia, July 8-13, 2004*. IAU Symposium, No. 224. Cambridge, UK: Cambridge University Press. pp. 131–138.
- Smalley B. 2005. Teff and log g determinations. *Memorie della Societa Astronomica Italiana Supplementi*. 8:130.
- Straumit I, Tkachenko A, Gebruers S, Audenaert J, Xiang M, Zari E, et al. 2022. Zeta-Payne: A fully automated spectrum analysis algorithm for the milky way mapper program of the SDSS-V survey. *AJ*. 163(5):236.
- Tabernero HM, Marfil E, Montes D, González Hernández JI. 2022. STEPARYN: A Bayesian code to infer stellar atmospheric parameters using spectral synthesis. *A&A*. 657:A66.
- Takeda Y, Kawanomoto S, Ohishi N, Kang D-I, Lee B-C, Kim K-M, et al. 2018. Photospheric carbon, nitrogen, and oxygen abundances of A-type main-sequence stars*. *Publ Astron Soc Jpn*. 70(5):91.
- Ting Y-S, Conroy C, Rix H-W, Cargile P. 2019. The Payne: self-consistent ab initio fitting of stellar spectra. *APJ*. 879(2):69.
- Tonry J, Davis M. 1979. A survey of galaxy redshifts. I. Data reduction techniques. *AJ*. 84:1511–1525.
- Wu J. 2017. Introduction to convolutional neural networks. In: *National Key Lab for Novel Software Technology*. China: Nanjing University, vol. 5, No. 23, pp. 495.
- Xiong S, Li X, Liao C. 2022. A model RRNet for spectral information exploitation and LAMOST medium-resolution spectrum parameter estimation. arXiv:2205.15490.
- Zorec J, Frémat Y, Domiciano de Souza A, Royer F, Cidale L, Hubert AM, et al. 2017. Critical study of the distribution of rotational velocities of Be stars. II: Differential rotation and some hidden effects interfering with the interpretation of the $V \sin i$ parameter. *A&A*. 602:A83.
- Zorec J, Royer F. 2012. Rotational velocities of A-type stars. IV. Evolution of rotational velocities. *A&A*. 537:A120.

Appendix

Table A1: Predicted values for T_{eff} , $\log g$, $[M/H]$, and $v_e \sin i$ for A stars with the median and closest values from Vizier catalogue

HIP	HD	T_{eff} (K)	T_{eff}^c (K)	T_{eff}^m (K)	$\log g$ (dex)	$\log g^c$ (dex)	$\log g^m$ (dex)	$[M/H]$ (dex)	$[X/H]^c$ (dex)	$[M/H]^m$ (dex)	$v_e \sin i$ (km/s)	$v \sin i^c$ (km/s)	$v \sin i^m$ (km/s)
HIP100108	HD193369	10,109	7,718	10,100	4.08	4.30	4.29	0.14	0.04	0.04	120.4	102.0	110.0
HIP102098	HD197345	7,081	7,823	7,572	2.22	2.51	2.13	0.61	0.06	0.48	31.3	34.7	34.7
HIP102208	HD199095	10,610	8,934	10,500	4.03	3.95	3.95	0.03	0.0	0.00	27.4	32.0	30.0
HIP103298	HD199254	7,842	8,145	7,900	3.37	4.01	3.50	-0.24	-0.2	-0.40	165.8	148.0	159.0
HIP104139	HD200761	9,959	9,595	10,001	3.74	4.11	4.00	0.28	0.26	0.26	145.6	104.0	130.0
HIP106297	HD205117	10,091	9,370	9,800	4.02	3.90	4.00	-0.10	0.00	-0.10	138.5	83.5	90.0
HIP10670	HD14055	10,174	9,340	10,772	4.17	4.08	4.19	-1.31	-0.58	-1.20	233.2	246.0	240.0
HIP10793	HD14252	8,638	8,380	8,749	3.35	4.74	3.40	-0.01	-0.05	0.00	23.5	22.0	25.0
HIP108875	HD209459	10,307	10,093	10,350	3.16	3.55	3.48	-0.95	-0.15	-0.42	2.0	11.0	3.8
HIP109521	HD210715	8,099	7,901	8,200	4.01	4.13	4.09	0.15	-0.10	-0.01	155.5	138.0	144.0
HIP111123	HD213320	10,826	10,125	10,864	3.79	4.05	3.76	1.11	0.41	0.49	22.1	21.0	23.0
HIP111169	HD213558	9,852	9,197	9,840	4.23	4.00	4.20	0.19	-0.28	0.00	149.1	128.0	150.0
HIP112029	HD214923	10,396	11,032	10,723	3.26	3.87	3.50	-0.24	0.00	-0.30	189.6	162.0	185.0
HIP112051	HD214994	9,834	9,452	9,866	3.67	3.68	3.65	1.44	0.08	0.42	5.1	10.0	5.0
HIP114745	HD219485	10,361	9,396	10,000	3.81	3.82	3.81	0.05	0.00	0.03	25.5	23.0	25.0
HIP11484	HD15318	10,790	10,308	10,900	3.64	4.00	3.48	0.00	-0.10	-0.04	61.7	57.0	65.0
HIP12706	HD016970	8,587	8,407	8,551	4.29	4.18	4.30	-0.13	-0.01	-0.01	192.0	186.0	190.0
HIP1366	HD1280	8,887	8,697	8,857	4.05	3.89	4.00	0.39	-0.69	0.14	101.9	102.0	102.0
HIP1473	HD1404	8,728	8,332	8,770	4.17	4.18	4.17	0.28	-0.09	0.05	138.3	119.0	123.0
HIP15154	HD20149	9,661	8,631	9,800	3.43	3.65	3.50	0.05	0.00	0.06	22.1	23.0	23.0
HIP16322	HD21686	10,199	9,468	10,000	3.61	4.00	3.67	-0.22	-0.2	-0.40	237.9	244.0	244.0
HIP17791	HD23763	8,581	8,441	8,591	4.33	4.03	4.10	0.33	-0.14	0.01	139.5	104.0	110.0
HIP18717	HD25175	10,460	8,034	10,500	3.44	3.83	3.59	-0.10	-0.51	-0.16	56.9	55.0	55.0
HIP19949	HD26764	10,123	8,215	9,825	3.57	3.39	3.67	-0.66	-0.65	-0.65	241.7	229.0	249.0
HIP20542	HD27819	8,056	7,957	8,050	4.18	3.96	4.11	0.44	-0.07	0.20	50.1	42.0	43.3
HIP20542	HD27819	7,799	7,957	7,800	3.67	3.96	3.70	0.13	-0.07	0.17	44.5	42.0	43.3
HIP20635	HD027934	7,737	8,105	7,800	3.35	3.81	3.40	0.35	-0.01	0.05	84.0	85.0	85.0
HIP20901	HD28355	7,170	7,705	7,592	3.95	4.00	3.97	0.23	0.30	0.20	89.9	105.0	90.0
HIP20901	HD028355	6,823	7,705	6,262	3.23	4.00	3.22	0.13	0.30	0.20	92.7	105.0	92.8
HIP21029	HD28527	7,466	8,086	7,700	3.58	3.91	3.69	0.09	0.13	0.10	66.1	86.0	70.0
HIP21589	HD29388	8,120	8,100	8,200	3.64	3.88	3.69	0.27	-0.05	0.13	81.3	86.8	80.0
HIP21683	HD029488	7,731	7,947	7,800	3.76	3.80	3.80	0.23	0.09	0.10	137.7	128.0	128.3
HIP21683	HD29488	7,687	7,947	7,614	3.46	3.80	3.67	0.02	0.09	0.09	141.9	128.0	128.3
HIP23497	HD32301	7,795	7,863	7,800	3.66	3.88	3.80	0.53	-0.01	0.15	130.4	124.5	131.0
HIP24340	HD33641	7,536	7,560	7,560	3.96	3.92	3.96	0.19	-0.03	0.12	94.8	84.5	92.0
HIP29997	HD042818	10,830	9,370	10,834	4.02	4.16	4.03	-0.57	0.30	0.30	265.6	255.0	260.0
HIP30060	HD043378	10,278	9,120	9,580	4.13	4.10	4.15	-0.12	-0.30	-0.10	45.3	45.5	45.0
HIP32104	HD48097	10,091	7,508	9,463	4.31	4.10	4.34	0.00	-0.10	-0.01	120.0	101.0	110.0
HIP32349	HD48915	9,554	9,900	9,580	4.14	4.35	4.20	0.45	0.33	0.50	18.9	16.0	18.0
HIP32921	HD49908	10,035	5,685	10,200	3.48	3.52	3.52	-0.34	-0.21	-0.35	154.2	117.0	140.0
HIP36145	HD58142	9,340	9,462	9,266	3.30	3.67	3.55	0.12	0.00	0.00	21.0	18.6	19.0
HIP41152	HD070313	8,747	8,038	8,720	4.05	4.00	4.03	0.46	-0.48	-0.01	119.1	112.0	114.0
HIP42028	HD72660	9,160	9,513	9,200	3.66	4.00	3.60	0.26	0.10	0.21	4.1	9.0	5.0
HIP4436	HD5448	8,163	7,118	8,222	4.29	3.81	4.20	0.24	-0.17	0.10	68.7	75.0	69.3
HIP45493	HD079439	6,751	7,630	7,450	4.09	4.04	4.10	-0.46	-0.04	-0.5	175.4	159.0	159.0
HIP50448	HD88983	7,628	7,890	7,600	3.73	3.89	3.89	-0.19	-0.19	-0.18	126.1	114.0	133.0
HIP50933	HD89822	9,661	10,000	9,741	3.65	3.80	3.66	0.48	0.15	0.46	3.9	10.0	4.6
HIP51200	HD090470	8,241	7,845	8,337	4.01	4.20	4.20	0.06	-0.01	-0.01	125.2	90.0	110.0
HIP52422	HD092769	7,100	6,990	7,600	4.42	4.13	4.30	-0.48	-0.15	-0.60	223.7	207.0	212.0
HIP5310	HD006695	8,773	8,304	8,720	3.99	4.30	3.91	0.07	-0.20	-0.01	164.2	149.0	150.0
HIP53485	HD94766	7,927	7,908	7,917	4.56	4.06	4.21	0.12	-0.05	0.00	94.7	85.0	85.0

(Continued)

Table A1: Continued

HIP	HD	T_{eff} (K)	T_{eff}^c (K)	T_{eff}^m (K)	$\log g$ (dex)	$\log g \ g^c$ (dex)	$\log g^m$ (dex)	$[M/H]$ (dex)	$[X/H]^c$ (dex)	$[M/H]^m$ (dex)	$v_e \sin i$ (km/s)	$v \sin i^c$ (km/s)	$v \sin i^m$ (km/s)
HIP54326	HD96399	7,414	6,662	7,400	3.62	3.72	3.40	-0.39	-0.49	-0.40	78.0	70.0	70.0
HIP54425	HD96681	7,963	7,638	7,829	3.41	3.66	3.40	-0.03	-0.14	-0.01	79.1	80.0	80.0
HIP55263	HD98377	8,813	8,297	8,800	4.68	4.01	4.13	-0.11	-0.10	-0.10	55.3	50.0	50.0
HIP5542	HD6961	7,578	7,962	7,597	3.74	3.64	3.80	0.51	-0.20	0.11	103.3	103.0	103.0
HIP55488	HD98747	7,056	7,136	6,992	4.03	3.91	4.15	-0.47	-0.12	-0.20	39.0	35.0	35.0
HIP56429	HD100518	7,942	7,637	7,986	3.60	3.61	3.50	-0.13	-0.16	-0.02	8.2	11.2	8.0
HIP57743	HD102841	7,173	7,400	7,181	4.41	3.70	4.55	-0.28	-0.30	-0.30	123.5	90.0	90.0
HIP59923	HD106887	7,823	8,291	7,900	3.93	4.20	3.80	0.46	0.21	0.21	86.2	82.0	84.1
HIP59988	HD106999	8,109	6,519	8,116	4.14	4.07	4.12	0.05	-0.21	0.08	50.4	47.7	51.4
HIP60327	HD107655	9,153	8,607	9,281	3.78	4.00	3.97	0.79	-0.09	0.08	56.1	46.0	50.0
HIP62874	HD112002	8,045	7,716	8,000	4.15	3.99	4.00	0.11	-0.45	0.10	54.7	50.0	50.0
HIP65304	HD116379	7,993	5,848	8,000	3.82	4.25	3.80	0.08	-0.27	-0.02	89.2	80.0	80.0
HIP65466	HD116706	8,907	8,480	8,909	3.92	3.93	3.93	0.35	-0.20	-0.01	56.3	54.0	55.0
HIP6686	HD8538	7,945	7,980	7,980	3.72	3.61	3.73	0.01	-0.45	-0.11	127.6	110.0	123.0
HIP67004	HD119537	8,740	8,661	8,661	3.97	3.99	3.99	0.20	-0.44	0.03	17.9	13.5	16.4
HIP73156	HD132145	9,434	9,230	9,376	3.95	4.13	4.00	-0.24	0.00	0.00	15.3	15.0	15.0
HIP75043	HD136729	8,295	8,247	8,279	3.88	4.19	3.85	-0.33	0.09	-0.30	161.3	159.0	161.0
HIP76267	HD139006	10,635	9,515	10,900	3.82	3.86	3.82	-0.26	0.20	-0.01	142.5	133.5	139.0
HIP78554	HD143894	9,246	8,652	9,226	3.97	3.93	3.93	0.28	0.38	0.38	149.2	128.0	130.0
HIP79332	HD145647	9,674	7,645	9,560	3.93	3.41	3.95	-0.40	-0.30	-0.36	46.8	43.0	45.0
HIP84036	HD155375	8,704	8,477	8,700	4.49	4.06	4.08	0.40	0.20	0.22	28.1	27.9	28.0
HIP84821	HD157087	8,592	8,185	8,600	3.38	3.10	3.44	0.11	-0.05	0.00	8.9	15.0	12.0
HIP85666	HD158716	8,593	8,068	8,600	3.82	4.26	3.82	0.17	-0.13	0.00	5.1	15.0	6.0
HIP8903	--	8,107	8,352	8,061	3.88	3.94	3.90	0.34	0.08	0.16	70.8	71.6	71.6
HIP91262	HD172167	9,608	9,485	9,657	3.93	3.96	3.93	-0.51	-0.54	-0.50	23.2	23.0	23.0
HIP92396	HD174567	10,395	9,208	10,500	3.46	3.55	3.50	0.44	0.00	0.15	9.6	15.0	12.0
HIP93526	HD176984	9,876	8,723	9,880	3.40	3.47	3.44	-0.10	-0.14	0.00	28.9	24.2	30.0
HIP9480	HD012111	7,586	7,700	7,700	3.99	4.02	3.95	0.04	-0.31	-0.21	71.2	71.6	71.6
HIP97229	HD186689	7,466	7,906	7,700	4.01	4.21	4.21	-0.10	-0.04	-0.05	32.5	31.0	31.0
HIP9977	HD013041	8,420	8,216	8,309	3.72	3.86	3.77	-0.41	-0.45	-0.40	164.8	133.0	135.0
—	HD23924	7,826	7,782	7,850	3.94	4.00	3.94	0.35	0.01	0.38	36.0	44.8	33.0

Table A2: Predicted values for T_{eff} , $\log g$, $[M/H]$, and $v_e \sin i$ for FGK stars with the median and closest values from Vizier catalogue

Star ID	T_{eff} (K)	T_{eff}^c (K)	T_{eff}^m (K)	$\log g$ (dex)	$\log g^c$ (dex)	$\log g^m$ (dex)	$[M/H]$ (dex)	$[X/H]^c$ (dex)	$[M/H]^m$ (dex)	$v_e \sin i$ (km/s)	$v \sin i^c$ (km/s)	$v \sin i^m$ (km/s)
HIP10138	5,194	5,188	5,195	4.91	4.56	4.91	0.01	-0.23	-0.09	7.0	2.3	3.9
HIP102422	4,937	4,971	4,940	2.54	3.40	2.99	0.30	-0.18	0.13	4.7	3.4	4.8
HIP105858	5,909	6,159	5,910	3.47	4.35	3.92	-1.10	-0.67	-0.84	24.0	3.7	10.0
HIP10644	5,871	5,702	5,845	3.92	4.29	3.92	-0.75	-0.43	-0.58	31.6	4.7	10.0
HIP10798	5,186	5,373	5,286	4.52	4.61	4.53	-0.84	-0.47	-0.80	8.8	2.7	3.6
HIP109176	6,664	6,479	6,693	3.72	4.23	4.02	-0.21	-0.10	-0.19	20.5	6.2	10.0
HIP110109	6,106	5,850	6,019	3.74	4.39	4.13	-0.70	-0.21	-0.44	8.3	2.0	2.7
HIP114622	4,755	4,829	4,749	2.12	4.50	2.59	0.92	0.05	0.20	9.0	2.0	8.0
HIP116771	6,273	6,186	6,279	3.58	4.12	3.75	-0.30	-0.14	-0.27	11.1	6.7	10.0
HIP12777	6,328	6,264	6,329	3.66	4.32	3.22	-0.16	-0.01	-0.15	12.6	8.9	10.2
HIP12843	5,523	6,371	6,144	3.74	4.29	4.00	0.15	0.05	0.15	25.0	25.6	25.0
HIP13402	5,171	5,180	5,170	4.54	4.56	4.55	0.62	0.08	0.21	9.9	4.9	10.0
HIP14632	6,340	5,963	6,045	3.61	4.16	3.35	0.66	0.09	0.29	8.5	4.3	10.0
HIP14879	6,160	6,170	6,165	3.50	3.95	3.57	-0.40	-0.21	-0.35	10.5	4.4	7.3
HIP15330	6,071	5,720	5,854	4.28	4.53	4.30	-0.84	-0.22	-0.34	12.2	2.7	3.0
HIP15371	6,155	5,866	6,066	3.96	4.48	4.22	-0.77	-0.23	-0.34	9.1	2.6	3.0
HIP15457	5,908	5,718	5,908	3.60	4.50	4.33	-0.16	0.06	-0.16	10.4	5.2	8.0
HIP15510	6,198	5,401	6,041	4.51	4.45	4.50	-0.52	-0.40	-0.49	7.0	1.5	4.0
HIP1599	6,234	5,957	6,151	3.70	4.42	4.02	-0.43	-0.19	-0.45	16.4	3.0	15.0
HIP16537	5,039	5,084	5,034	4.51	4.57	4.51	0.27	-0.11	0.06	16.9	2.5	15.0
HIP16852	6,183	5,997	6,200	3.47	4.09	3.85	-0.21	-0.09	-0.21	8.3	4.3	8.0
HIP171	5,853	5,438	5,798	4.40	4.38	4.40	-0.97	-0.79	-0.98	15.1	3.0	5.0
HIP17378	4,734	5,037	4,750	2.35	3.77	3.27	0.36	0.10	0.25	24.7	2.3	15.0
HIP17420	4,957	4,979	4,957	3.86	4.57	4.41	0.36	-0.11	0.10	9.4	3.0	5.7
HIP2021	6,042	5,848	5,924	3.42	3.95	3.45	0.00	-0.09	0.00	9.2	3.3	5.0
HIP22263	6,300	5,834	6,131	3.72	4.49	4.30	-0.48	0.01	-0.19	13.0	3.2	6.4
HIP22449	5,857	6,424	5,820	3.52	4.29	3.77	0.02	0.00	0.02	18.3	17.2	18.5
HIP23311	4,790	4,790	4,790	2.09	4.55	4.23	1.18	0.28	0.44	21.4	2.0	5.2
HIP23693	5,838	6,153	5,727	3.66	4.44	4.06	-0.32	-0.17	-0.34	17.7	15.4	17.3
HIP24813	6,167	5,858	5,979	3.67	4.20	3.98	0.51	0.05	0.26	3.7	2.0	3.1
HIP26779	5,301	5,243	5,300	4.27	4.50	4.26	0.49	0.09	0.21	15.5	2.5	5.4
HIP27072	6,381	6,306	6,384	3.64	4.31	3.99	-0.23	-0.05	-0.22	12.7	7.7	10.4
HIP27913	5,892	5,949	5,895	3.74	4.44	4.21	-0.40	-0.03	-0.18	13.0	8.9	10.7
HIP29271	5,628	5,569	5,621	3.70	4.43	4.20	0.77	0.10	0.25	18.4	1.8	2.3
HIP3093	5,018	5,221	5,024	4.11	4.49	4.15	0.51	0.15	0.26	7.6	1.2	8.0
HIP37279	6,770	6,596	6,775	3.47	4.00	3.74	-0.27	-0.01	-0.29	10.7	5.5	10.1
HIP37349	4,812	4,932	4,826	2.74	4.60	2.68	0.83	-0.01	0.09	6.6	3.8	5.6
HIP3765	5,024	4,978	5,020	4.82	4.61	4.82	0.06	-0.24	-0.04	9.7	2.0	6.3
HIP3821	6,022	5,925	6,034	3.65	4.40	4.00	-0.59	-0.28	-0.60	10.5	2.8	9.2
HIP40693	5,428	5,402	5,428	3.79	4.48	3.66	0.16	-0.03	0.14	9.0	2.0	6.7
HIP4148	4,688	4,952	4,822	3.50	4.61	4.49	0.32	-0.11	0.00	8.7	1.8	4.5
HIP41926	5,080	5,243	5,155	4.69	4.56	4.68	-0.73	-0.40	-0.48	8.8	2.7	6.8
HIP42438	5,765	5,876	5,759	3.66	4.47	4.40	-0.35	-0.06	-0.29	13.8	10.0	13.2
HIP42808	5,018	4,969	5,005	4.73	4.60	4.66	0.75	-0.03	0.10	8.9	3.8	9.6
HIP46853	6,217	6,336	6,225	3.29	3.87	3.50	-0.42	-0.16	-0.31	12.3	8.6	10.0
HIP51459	6,301	6,156	6,301	3.57	4.39	3.96	-0.32	-0.13	-0.28	9.3	4.3	10.0
HIP5336	5,335	5,316	5,336	4.49	4.49	4.49	-1.15	-0.83	-0.98	19.3	5.4	15.0
HIP53721	6,186	5,882	6,140	3.70	4.30	4.07	0.52	0.01	0.31	6.2	2.8	5.6
HIP544	5,546	5,481	5,551	3.44	4.55	3.99	0.64	0.12	0.22	8.9	4.1	6.2
HIP56452	5,128	5,158	5,129	4.80	4.56	4.68	-0.92	-0.38	-0.57	8.1	3.5	6.7
HIP56997	5,605	5,507	5,609	3.71	4.54	3.45	-0.48	-0.05	-0.50	33.5	2.4	15.0
HIP57443	5,982	5,629	5,970	4.21	4.44	4.21	-0.83	-0.29	-0.66	10.3	0.7	3.0
HIP57757	6,470	6,109	6,246	3.55	4.10	3.86	0.52	0.13	0.33	8.3	4.0	10.0
HIP58576	5,332	5,510	5,361	3.37	4.40	3.65	0.94	0.25	0.35	8.4	2.0	5.2

(Continued)

Table A2: Continued

Star ID	T_{eff} (K)	T_{eff}^c (K)	T_{eff}^m (K)	$\log g$ (dex)	$\log g^c$ (dex)	$\log g^m$ (dex)	$[M/H]$ (dex)	$[X/H]^c$ (dex)	$[M/H]^m$ (dex)	$v_e \sin i$ (km/s)	$v \sin i^c$ (km/s)	$v \sin i^m$ (km/s)
HIP61317	6,063	5,881	6,061	3.70	4.39	3.38	-0.56	-0.19	-0.39	2.1	2.8	2.1
HIP61941	5,502	6,875	5,433	3.64	4.26	3.88	-0.40	-0.09	-0.44	28.6	28.3	29.7
HIP64241	5,687	6,343	5,250	3.64	4.09	3.99	0.01	-0.23	0.0	20.9	19.9	20.5
HIP64394	6,517	6,009	6,225	3.72	4.40	4.24	0.06	0.04	0.06	10.7	4.4	10.0
HIP64924	5,660	5,558	5,660	3.75	4.40	3.50	-0.17	-0.01	-0.13	8.4	2.2	8.0
HIP67927	6,076	6,047	6,078	3.49	3.78	3.53	0.82	0.25	0.47	15.5	13.5	15.4
HIP68184	4,776	4,831	4,792	2.20	4.55	4.38	1.00	0.12	0.33	25.4	1.3	9.0
HIP71681	5,203	5,551	5,203	4.11	4.31	4.16	0.57	0.21	0.27	11.3	2.7	4.5
HIP72659	5,616	5,483	5,595	4.23	4.56	4.37	-0.67	-0.14	-0.83	15.7	4.6	16.0
HIP72848	5,290	5,260	5,291	4.10	4.53	4.11	0.60	0.08	0.14	9.5	4.5	6.3
HIP73695	6,160	5,495	6,200	3.78	4.23	4.10	-0.54	-0.30	-0.42	6.2	3.7	3.7
HIP7513	6,296	6,155	6,269	3.65	4.13	3.90	0.24	0.09	0.19	13.7	9.6	11.9
HIP77257	6,206	5,901	6,131	3.57	4.15	4.00	-0.06	-0.01	-0.05	8.3	3.1	10.0
HIP7751	4,969	5,043	4,970	4.58	4.63	4.61	-0.27	-0.20	-0.26	8.5	3.9	6.8
HIP77952	5,492	7,107	5,377	2.77	4.16	3.76	0.11	-0.25	-0.20	79.2	75.0	75.0
HIP78072	6,117	6,278	6,146	3.67	4.13	3.91	-0.36	-0.18	-0.32	13.9	10.0	11.9
HIP78775	5,321	5,294	5,321	4.72	4.58	4.71	-0.85	-0.67	-0.76	6.6	2.0	7.0
HIP7918	6,232	5,880	6,179	3.73	4.30	4.10	0.68	0.0	0.2	7.1	3.2	5.0
HIP79190	5,033	5,060	5,024	4.91	4.55	4.66	-0.18	-0.37	-0.21	8.7	1.6	5.0
HIP79672	6,213	5,799	6,053	3.71	4.43	4.16	-0.32	0.04	-0.29	8.3	2.5	8.3
HIP7981	5,154	5,201	5,155	3.34	4.50	3.25	0.13	-0.04	0.12	10.4	1.7	10.0
HIP80337	6,525	5,882	6,060	3.68	4.50	4.40	-0.30	0.03	-0.19	17.5	1.6	3.9
HIP80686	6,417	6,090	6,459	3.68	4.45	4.24	-0.30	-0.08	-0.19	10.8	3.2	3.3
HIP8102	5,456	5,330	5,459	4.57	4.51	4.57	-0.74	-0.52	-0.68	3.4	1.8	3.5
HIP81300	5,087	5,272	5,080	4.15	4.57	4.39	0.07	0.02	0.07	8.0	2.0	4.1
HIP81693	5,994	5,764	5,906	3.20	3.74	3.53	0.77	0.02	0.10	8.4	4.3	10.0
HIP8362	5,257	5,374	5,257	3.56	4.54	4.30	0.01	0.05	0.01	7.2	1.3	10.0
HIP84405	5,009	5,089	5,007	4.80	4.60	4.64	-0.48	-0.23	-0.38	7.7	2.5	5.1
HIP84720	5,285	5,209	5,273	4.76	4.53	4.61	-0.77	-0.34	-0.46	8.6	1.9	4.5
HIP84862	6,270	5,703	6,079	3.90	4.26	3.80	-0.70	-0.37	-0.79	2.9	1.7	3.0
HIP85235	5,072	5,290	5,194	4.61	4.57	4.61	-0.74	-0.44	-0.52	5.0	1.3	3.4
HIP86036	6,490	5,893	6,077	3.65	4.39	4.13	0.11	-0.03	0.08	13.5	4.5	6.0
HIP86400	4,863	4,883	4,864	2.24	4.52	4.30	0.50	-0.08	0.17	13.7	2.5	4.1
HIP86974	5,361	5,508	5,342	2.86	3.97	3.72	0.82	0.23	1.29	7.8	3.9	8.0
HIP88601	5,174	5,250	5,182	3.82	4.54	4.30	0.30	-0.01	0.19	11.0	3.5	13.0
HIP88972	5,034	5,000	5,035	4.78	4.50	4.74	0.37	-0.17	0.07	5.0	2.1	4.1
HIP91438	5,918	5,636	5,884	4.26	4.49	4.25	-0.90	-0.24	-0.35	34.1	2.8	4.0
HIP96100	5,261	5,271	5,260	4.47	4.55	4.49	-0.70	-0.22	-0.43	7.2	2.3	6.7
HIP97944	5,052	4,767	5,081	2.13	4.20	2.00	0.93	-0.03	0.38	33.7	2.0	10.2
HIP98036	5,082	5,100	5,082	2.60	3.55	3.04	0.13	-0.15	-0.04	6.6	2.5	4.6
HIP99461	4,949	4,971	4,952	4.80	4.55	4.73	-0.10	-0.51	-0.21	9.9	1.8	3.9
HIP99825	5,233	5,091	5,179	4.14	4.51	4.37	0.46	0.00	0.14	18.0	2.0	4.3